

# RAM: Reachability Across Morphologies

**Tim Walter**

Department of Computer Engineering  
 Technical University Munich  
 Germany  
 tim.walter@tum.de

**Xinyu Chen**

German Electron Synchrotron  
 University of Hamburg  
 Germany  
 xinyu.chen@uni-hamburg.de

**Jonathan K ulz**

Department of Computer Engineering  
 Technical University Munich  
 Germany  
 jonathan.kuelz@tum.de

**Matthias Althoff**

Department of Computer Engineering  
 Technical University Munich  
 Germany  
 matthias.althoff@tum.de

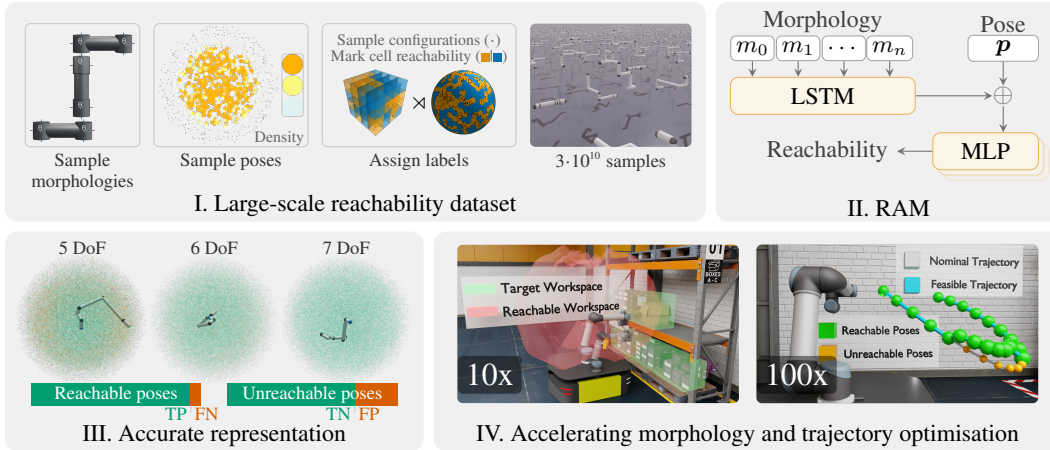


Figure 1: We present RAM, a surrogate model for robot reachability. Trained on a diverse dataset of thirty billion samples (I), the morphology-conditioned implicit neural representation (II) generalises accurately to unseen morphologies (III). Due to its differentiability and efficient inference, RAM can substantially accelerate downstream robotics tasks by replacing inverse kinematics (IV).

**Abstract:** Many stages of the robotic lifecycle, from morphology synthesis to operation, rely fundamentally on the reachable workspace. However, current methods for approximating workspaces are slow, imprecise, or tied to a single morphology. We introduce Reachability Across Morphologies (RAM): a morphology-conditioned, implicit neural representation that acts as a fast, differentiable surrogate for pose reachability, generalising to unseen morphologies while inherently accounting for self-collisions. To train RAM, we publish a large-scale dataset of  $3 \cdot 10^{10}$  samples generated solely from forward kinematics. Experiments show that our model achieves an  $F_1$ -score of 86% at nanosecond inference, outperforming the baseline by 14% while reducing inference time by three orders of magnitude. We further demonstrate speed-ups of one and two orders of magnitude for gradient-based morphology and trajectory optimisation, respectively. Website: <https://timwalter.github.io/ram>.

**Keywords:** Reachability, Implicit Neural Representations, Morphology Synthesis

## 1 Introduction

Tailoring robots to their operating environments through design optimisation, modular reconfiguration, or tool-use [1–3] commonly improves task performance, while reducing costs and complexity

compared to general-purpose solutions [1, 4–7]. Despite these advantages, a major computational hurdle in both the design and operation of novel morphologies is computing their workspace, which requires solving inverse kinematics and checking for self-collisions [8, 9]. Inverse kinematics do not admit analytical solutions for arbitrary kinematic chains [10, Chapter 6.2], so numerical or learning-based solvers must be employed, yet these are slow, sensitive to initialisation, and converge to a single joint configuration rather than characterising the full solution set [10, 11]. Moreover, exhaustive workspace evaluation requires querying millions of poses, making iterative design synthesis or reactive planning prohibitively slow.

Our key insight is that iterative tasks such as trajectory and morphology optimisation require only the existence of an inverse kinematics solution at each step, whereas the solution itself is only needed for the final result. While pre-computing workspaces has proven effective for individual robots [12–16], they must be recomputed for every morphology. We aim for a single, conditioned representation generalising across different morphologies. To this end, we propose Reachability Across Morphologies (RAM): a fast, differentiable surrogate model for reachability. RAM is a morphology-conditioned, implicit neural representation [17] that encodes the reachable workspace through an occupancy network [18]. By shifting to a learned representation, we enable reachability evaluation in nanoseconds and ensure that the predicted workspace varies smoothly across the design space. Learning the intricate relationship between morphology and reachability requires large amounts of training data, which we efficiently generated without the computational overhead and uncertainty of inverse kinematics.

We demonstrate that RAM represents diverse workspaces with high fidelity, outperforming the generalised inverse kinematics baseline [19] in both accuracy and inference latency. Furthermore, we show that our data generation produces reliable labels and scales to billions of samples. Finally, we demonstrate the practical utility of RAM by showing substantial acceleration in gradient-based morphology and trajectory optimisation over traditional numerical methods.

In summary, our core contributions are:

- **RAM:** a novel, morphology-conditioned implicit neural representation based on an occupancy network that acts as a fast, differentiable surrogate model for pose reachability;
- **Large-scale Reachability Dataset:** A public dataset of  $3 \cdot 10^{10}$  samples across  $3 \cdot 10^4$  unique robot morphologies generated solely from forward kinematics and self-collision queries, with pose sampling restricted to geometrically plausible regions to maximise learning signal;
- **Accelerating Morphology & Trajectory Optimisation:** Our differentiable surrogate model enables gradient-based morphology and trajectory optimisation at significantly lower computational costs compared to inverse kinematics.

## 2 Problem Statement

Our objective is to learn the reachability map  $\Psi : \mathcal{M} \times \text{SE}(3) \rightarrow \{0, 1\}$ . This map identifies whether a pose  $\mathbf{P} \in \text{SE}(3)$  lies in the reachable workspace of a morphology  $\mathbf{M} \in \mathcal{M}$ . The reachable workspace is the set of all end-effector poses attained by the forward kinematics  $f : \mathcal{M} \times \mathcal{T}^n \rightarrow \text{SE}(3)$  over all collision-free joint configurations  $\boldsymbol{\theta} \in \mathcal{T}^n$ , where  $\mathcal{T}^n = (\mathcal{S}^1)^n$  and  $n$  is the number of joints. Formally,  $\Psi(\mathbf{M}, \mathbf{P}) = 1$  if and only if the fibre, i.e., the inverse kinematics solution set,  $f^{-1}(\mathbf{M}, \mathbf{P}) = \{\boldsymbol{\theta} \in \mathcal{T}^n \mid f(\mathbf{M}, \boldsymbol{\theta}) = \mathbf{P}\}$  admits a collision-free solution

$$\Psi(\mathbf{M}, \mathbf{P}) = \begin{cases} 1 & \text{if } \exists \boldsymbol{\theta} \in f^{-1}(\mathbf{M}, \mathbf{P}) : c(\mathbf{M}, \boldsymbol{\theta}) \\ 0 & \text{else,} \end{cases} \quad (1)$$

where  $c$  holds if and only if morphology  $\mathbf{M}$  in configuration  $\boldsymbol{\theta}$  is not in self-collision.

## 3 Related Work

*Inverse Kinematics.* Traditionally, reachability is determined by solving the inverse kinematics problem directly. Analytical solvers such as IKfast [20] and the Efficient Analytical Inverse Kinematics

toolbox (EAIK) [21] are reliable, fast, and yield the complete solution set  $f^{-1}(M, P)$  for morphologies with decomposable topologies or fewer than five degrees of freedom (DoF). Numerical solvers apply to arbitrary morphologies by iteratively minimising a pose residual  $r(P, f(M, \theta))$  over  $\theta$ , typically with multiple random restarts to improve coverage of the solution space [22–24]. Learning-based models of inverse kinematics [1, 19, 25–27] trade accuracy for speed, yet still predict a joint configuration  $\theta$ , which is a richer output than the reachability map  $\Psi$  requires.

*Reachability Maps.* For fixed morphologies, pre-computing workspaces accelerates reachability assessment. Traditional approaches range from extracting workspace boundaries through singularity analysis [28] to compact geometric approximations such as ellipsoids [29]. However, singularity analysis requires enumerating joint limit combinations that grow combinatorially with the number of joints, limiting applicability to five DoF, while geometric approximations sacrifice fidelity for compactness, motivating discretised alternatives. Voxel-based capability maps were first introduced by Zacharias et al. [12] to pre-calculate reachability over the entire workspace via inverse kinematics. Subsequent work [13–16] extended them to incorporate full SE(3) poses and self-collision measures, and expedited the computation by convolving reachability maps of single links. Despite these advances, voxel-based methods remain fundamentally memory-intensive and tied to a single morphology.

*Implicit Neural Representations.* Implicit neural representations have emerged as a powerful alternative to discretisation by encoding continuous functions within the weights of a neural network [17]. In computer vision and graphics, representations such as neural signed distance functions [30], neural radiance fields [31], and occupancy networks [18] have demonstrated that neural networks that take spatial coordinates as input can represent complex geometries and volumetric scenes with high fidelity at a fraction of the memory costs of voxels. This paradigm has recently transitioned to robotics [32], where such representations are used to encode robot geometry [33] and configuration-space distance fields [34]. Prior work has learned surrogate reachability models for single morphologies [35–37], with Gienger et al. [35] incorporating self-collisions and Murooka et al. [36] training solely from forward kinematics. Chen et al. [38] explore morphology-conditioning but remain limited to 3D positions and a small design space. Full SE(3) reachability encompasses orientation in addition to position, yielding a substantially larger and non-Euclidean space. The resulting workspaces exhibit far greater topological variation than position-only workspaces, and no prior work provides a morphology-conditioned neural representation of the full SE(3) reachable workspace that inherently accounts for self-collisions.

## 4 Reachability Across Morphologies (RAM)

We treat workspace representation as binary occupancy classification. Our data synthesis first samples a morphology (Section 4.1), determines its geometrically plausible poses (Section 4.2), and assigns reachability labels (Section 4.3). A reachability classifier is then trained to implicitly encode the workspace in its decision boundary (Section 4.4).

### 4.1 Morphology Sampling

We consider serial kinematic chains of the form

$$\text{base} \rightarrow \text{joint}_0 \rightarrow \text{link}_1 \rightarrow \text{joint}_1 \rightarrow \cdots \rightarrow \text{joint}_{n-1} \rightarrow \text{end effector}$$

composed of  $n \in \{5, 6, 7\}$  revolute joints covering the most practically relevant manipulator configurations that do not always admit analytical inverse kinematics. We restrict ourselves to morphologies that are:

1. **Operable:** The morphology must admit at least one configuration free of self-collisions.
2. **Non-degenerate:** We exclude degenerate designs, where degeneracy is defined as having fewer functional DoF  $n_{\text{func}}$  than nominal joints  $n_{\text{func}} < \min(6, n)$  [39].
3. **Conventional:** Successive joint axes are either parallel or orthogonal, and no more than two joints are co-located.

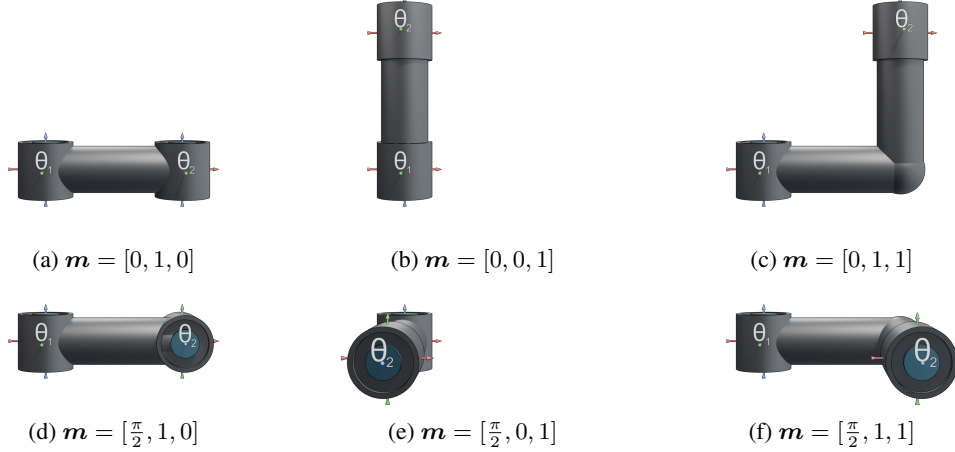


Figure 2: Example link types with columns representing length-only, offset-only, and both. The bottom row (d-f) introduces a twist to the respective types in the top row (a-c). Joint angles are zero.

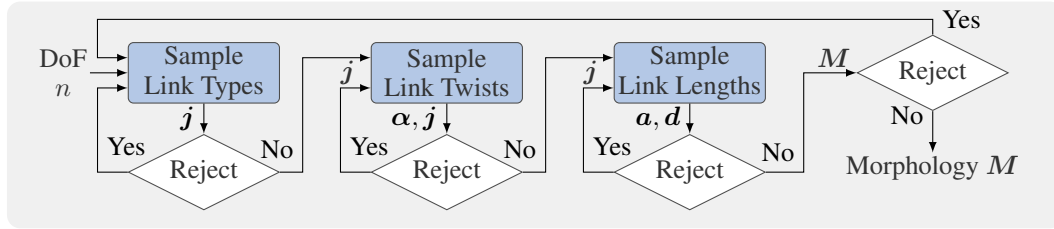


Figure 3: Hierarchical rejection sampling of morphologies. Each stage samples new parameters and passes accumulated ones to the next. Variables on arrows denote dependencies of their destination.

Modified Denavit-Hartenberg parameters [40] encode our kinematics as the sequence  $M = (m_0, \dots, m_{n-1}, m_{\text{eff}})$ , where  $m_i = [\alpha_{i-1} \ a_{i-1} \ d_i]$  encodes one link-joint pair via the link twist  $\alpha_{i-1} \in \{-\frac{\pi}{2}, 0, \frac{\pi}{2}\}$ , the link length  $a_{i-1} \in \mathbb{R}$ , and the link offset  $d_i \in \mathbb{R}$ . We collect all twists, lengths, and offsets into vectors  $\alpha \in \{-\frac{\pi}{2}, 0, \frac{\pi}{2}\}^n$ ,  $\mathbf{a} \in \mathbb{R}^n$ ,  $\mathbf{d} \in \mathbb{R}^n$  respectively. Since the workspace is topologically invariant to scale, we normalise without loss of generality to  $\sum_i \sqrt{a_i^2 + d_i^2} = 1$ . We assign a geometry to each pair by placing two capsules of radius  $r$  with lengths  $a_{i-1}$  and  $d_i$  along the  $x$ - and  $z$ -axes of each link-joint frame, enabling efficient self-collision checks. To prevent perpetual self-collisions, see Section A, we constrain  $a_{i-1}$  and  $d_i$  to  $\{0\} \cup [2r, 1]$ . Example morphologies induced by single links are shown in Figure 2.

The morphological constraints create a complex feasible region, making direct uniform sampling impractical. Therefore, we employ hierarchical rejection sampling outlined in Figure 3, which exploits the dependence of later parameters on earlier ones to check constraints early and discard violating candidates from a large parallel batch. This enables efficient generation and uniform coverage of the valid morphological space, which is necessary for unbiased training data. Section B details the sampling and rejection criteria.

## 4.2 Pose Sampling

We restrict pose sampling to geometrically plausible regions by excluding trivially unreachable positions outside the unit ball  $\mathbb{R}^3 \setminus \mathcal{B}^3$ , a consequence of the unit-size normalisation of the robot. Moreover, most poses in  $\mathcal{B}^3 \times \text{SO}(3)$ , where  $\times$  denotes the semi-direct product, are also unreachable: since the volume of  $\mathcal{B}^3$  concentrates near its boundary, uniformly sampled positions tend to lie at larger radii, where the robot must be nearly fully extended and can therefore only reach a highly restricted set of orientations. We therefore sample uniformly from the reduced pose space  $\mathcal{B}^3(t_0, r_{\text{mov}}) \times \text{SO}(3)$ , centred at the first joint position  $t_0$  with moveable length  $r_{\text{mov}} = 1 - \sqrt{a_0^2 + d_0^2} - \sqrt{a_{\text{eff}}^2 + d_{\text{eff}}^2}$ , and compose the result with the end-effector transformation

from Section E. Section D details uniform sampling on  $\mathcal{B}^3(t_0, r_{\text{mov}}) \times \text{SO}(3)$ . Figure 1-I depicts a typical sampling distribution. Morphologies with five DoF require special treatment, since their workspace is a five-dimensional submanifold of  $\text{SE}(3)$  and the aforementioned sampling would yield a severe class imbalance towards unreachable poses. We therefore supplement the pose-sampled data with samples drawn directly from the configuration space via forward kinematics.

### 4.3 Label Assignment

Rather than assessing each pose individually via inverse kinematics, we first approximate the reachable workspace and then determine reachability by checking whether a pose is contained within it. We employ the closed-world assumption [41], i.e., that any fact not explicitly observed is assumed false, which in our context implies that any pose not reached during a sufficiently dense sampling of the configuration space is considered unreachable. This necessitates a discretisation of  $\text{SE}(3) = \mathbb{R}^3 \times \text{SO}(3)$ , which we perform separately for  $\mathbb{R}^3$  and  $\text{SO}(3)$  by exploiting the semi-direct product structure. While the translation space  $\mathbb{R}^3$  is trivially split into cubic cells,  $\text{SO}(3)$  requires a more complex approach to avoid spherical distortion. We employ the technique of Leibrandt et al. [16], which discretises  $\text{SO}(3)$  via iterative tessellation of the 600-cell [42, P.249], the 4D analogue of the icosahedron, and pre-computes a lookup table for constant-time orientation indexing. Given the discretisation, we approximate the workspace by sampling joint configurations as detailed in Section C, evaluating the resulting forward kinematics, and discarding poses resulting in self-collision. Cells are marked as reachable if any valid pose is contained in them. Since a pose may admit multiple inverse kinematics solutions, a self-collision does not mark its cell as unreachable, since a collision-free solution may still exist. This tends to over-approximate the true workspace, akin to a dilation by the cell size, which may smooth the workspace boundary and ease learning. We label the poses sampled according to Section 4.2 with the label of their respective cell. Once the workspace is approximated, labelling a new pose requires only a constant-time cell lookup, making dataset extension computationally negligible.

### 4.4 Training & Architecture

To ensure a continuous rotation representation, we represent poses as  $\mathbf{p} = [\mathbf{t} \ \mathbf{q}]^T \in \mathbb{R}^9$ , where  $\mathbf{t} \in \mathbb{R}^3$  denotes the translation vector and  $\mathbf{q}$  is the continuous 6D rotation representation of Zhou et al. [43]. Since  $M$  is a variable-length sequence, we encode it into a fixed-size latent embedding using a long short-term memory (LSTM) [44] module. This embedding is concatenated with  $\mathbf{p}$  and passed through a multilayer perceptron (MLP) with sigmoid output, yielding the reachability probability

$$y = \text{RAM}(M, \mathbf{p}) = \text{MLP} \left( \left[ \begin{array}{c} \mathbf{p} \\ \text{LSTM}(M) \end{array} \right] \right). \quad (2)$$

The training minimises the binary cross entropy loss  $\mathcal{L}(l, y) = -(l \log(y) + (1 - l) \log(1 - y))$ , where  $l \in \{0, 1\}$  is the reachability label. Given the short sequences considered, we opt for an LSTM over a transformer-based encoder for its simplicity and lower computational overhead, with preliminary experiments showing comparable accuracy between the two. Section M summarises further architecture experiments, all of which performed worse or trained more slowly.

## 5 Experiments

We structured our experiments around three research questions:

- RQ1: Label fidelity.** How finely must  $\text{SE}(3)$  be discretised, and how many forward kinematics samples are required to achieve high-fidelity labels? (Section 5.1)
- RQ2: Representation Accuracy.** How accurately and efficiently does RAM represent workspaces of unseen morphologies? (Section 5.2)
- RQ3: Practical Utility.** Does RAM’s differentiability and fast inference accelerate morphology and trajectory optimisation? (Section 5.3)

Table 1: Effects of the discretisation granularity on workspace approximation.

Cell Distance	# Cells	Runtime (s)	$F_1$ -Score (%)
[0.158, 0.163]	231, 840	<1.00	74 $^{+2}_{-2}$
[0.080, 0.083]	11, 971, 800	<1.00	85 $^{+2}_{-2}$
[0.040, 0.042]	686, 811, 600	21.80 $^{+3.00}_{-3.00}$	91 $^{+1}_{-2}$
[0.021, 0.033]	29, 605, 439, 140	469.50 $^{+79.53}_{-6.75}$	90 $^{+2}_{-3}$

For all experiments, the forward kinematics pipeline of Section 4.3 labelled the training set, while test and validation labels were

$$l = \begin{cases} 1 & \text{if } \exists \theta \in \mathcal{Q} : \left( \|P - f(\mathbf{M}, \theta)\|_{\text{SE}(3)} < \epsilon \right) \wedge c(\mathbf{M}, \theta) \\ 0 & \text{else,} \end{cases} \quad (3)$$

where the solution set  $\mathcal{Q}$  was obtained from either EAIK [21] for analytically solvable kinematics or a collision-aware Levenberg-Marquardt solver with random restarts; and Section F defines the SE(3) norm. We computed all stochastic metrics per morphology and then aggregated across morphologies, reporting means and 95% confidence intervals over morphologies via bootstrapping.

### 5.1 Label Fidelity (RQ1)

We implemented a fast workspace approximation utilising accelerator-based implementations [45] to sample joint configurations, perform forward kinematics, and label the resulting poses at roughly  $5 \cdot 10^9$  configurations per minute on an Nvidia H100 GPU. The workspace approximation was considered complete once the true positive rate on the evaluation set, consisting of  $10^5$  poses, exceeded 95% or after 10 minutes of computation. We approximated the workspaces for 50 morphologies at the coarser granularity and 20 at the finest. Since each subdivision step of the 600-cell multiplies the number of SO(3) cells by  $\approx 2^3$  [16], only a coarse set of resolution levels is feasible; we matched the  $\mathbb{R}^3$  resolution accordingly. Table 1 reports discretisation metrics, the  $F_1$ -score, and runtime. Section G contains the detailed binary confusion matrix.

The  $F_1$ -score increased as expected with higher granularity due to the smaller cells, which decreased false positives. However, within the allocated computation time, not all approximations achieved 95% true positives at the highest granularity, leading to an increase in false negatives. Consequently, we used the discretisation with cell distance [0.040, 0.042], which achieves an  $F_1$ -score of 91% against the reference labels, establishing a practical ceiling on the accuracy achievable by RAM trained on these labels.

### 5.2 Accuracy of RAM (RQ2)

To train our model, we generated  $3 \cdot 10^{10}$  samples from  $3 \cdot 10^4$  distinct morphologies. We evaluated the representation accuracy across  $3 \cdot 10^2$  workspaces, each assessed with  $10^5$  poses sampled according to Section 4.2 and  $10^2$  boundary poses sampled along geodesics between reachable and unreachable poses. Section H provides dataset details and Section J hyperparameters. We compared our approach to Generative Graphical Inverse Kinematics (GGIK) [19], which, to our knowledge, is the only published baseline generalising reachability prediction across morphologies in SE(3). GGIK was trained using their out-of-distribution generalisation procedure [19, Sec. V.B], which required  $4 \cdot 10^6$  distinct samples from our morphological space, generating 32 solutions per pose to yield  $\mathcal{Q}$ . We set GGIK’s pose error threshold  $\epsilon$  to maximise the  $F_1$ -score on the validation set. Due to the slow inference, we were only able to validate GGIK on  $10^3$  poses per morphology. Table 2 shows the total training time, the inference time per sample, and the  $F_1$ -score; Section K reports the full confusion matrix. In addition, Figure 4 shows example workspace slices, generated as described in Section I.

Most transformations required to convert GGIK inputs and outputs were neither batched nor accelerator-friendly, accounting for 22 milliseconds of total inference time, compared to RAM’s 57 nanoseconds. However, even the sole GGIK query took 83 microseconds, which remains about three orders of magnitude slower than RAM due to the more complex architecture. Consequently, despite training on a dataset more than three orders of magnitude smaller, GGIK required a month of training compared to our 57 hours, driven by 360 epochs over a computationally expensive architecture. RAM also outperformed GGIK by at least 9% in  $F_1$ -score on both random and boundary poses. Since RAM was specifically designed and trained for reachability, it solves a simpler problem: GGIK predicts link positions that are often physically infeasible and require solving for joint configurations that best match the predictions. This introduces additional deviations and necessitates a high pose threshold of  $\epsilon \approx 0.2$ , within which many unreachable poses have reachable neighbours.

Table 2: Comparison of RAM and GGIK. Inference is from pose and morphology input to reachability output.

Classifier	Training (h)	Inference (s)	$F_1$ -Score (%)	
			Random	Boundary
RAM	57	$5.7 \cdot 10^{-8}$	$86_{-1}^{+1}$	$78_{-3}^{+3}$
GGIK	756	$2.2 \cdot 10^{-2}$	$72_{-1}^{+1}$	$69_{-2}^{+3}$

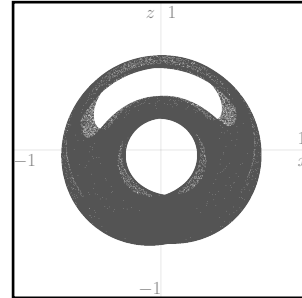
The over-approximation trend in RAM is consistent with its training data and the implicit smoothing of the MLP architecture [17], resulting in a majority of false positives among misclassified samples, as reported in Section K.

We also evaluated RAM out-of-distribution on morphologies with  $\{1-4, 8, 9\}$  DoF. RAM maintained  $F_1$ -scores above 78% for four, eight, and nine DoF, demonstrating robust generalisation to higher DoF. Performance dropped substantially below four DoF, with one and two DoF achieving  $F_1$ -scores of only 3% and 32%, respectively, likely because their workspaces have fundamentally different topologies from the training distribution. Since most poses are unreachable for low-DoF morphologies, the model gracefully defaults to predicting unreachable, which limits false positives at the cost of recall.

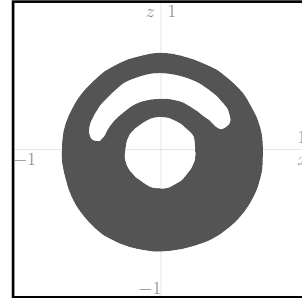
To explore the structure of the latent space, we projected  $3 \cdot 10^3$  latent vectors of random morphologies onto their principal components and computed Spearman correlations [46] with semantic morphological attributes. Across all principal components, the number of DoF showed the highest Spearman correlation of 86%, followed by the standard deviation of link lengths with 58%, indicating that the latent space is organised by kinematic complexity. We further applied Mantel tests [47] across all pairwise combinations of 50 morphologies, correlating latent similarity with both input and workspace similarity. Both correlations were statistically significant but modest: 34% for inputs and 28% for workspaces, likely reflecting the LSTM encoder’s small parameter count relative to the MLP decoder. Section K details the methodology and reports all correlation coefficients with confidence intervals and  $p$ -values.

### 5.3 Utility of RAM (RQ3)

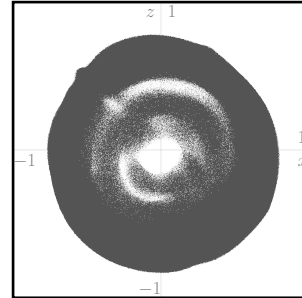
To exploit the differentiability of RAM, we employ a process pioneered in image classification [48–50] and optimise the inputs by backpropagating through the representation. As a baseline, we com-



(a) Labels.



(b) RAM.



(c) GGIK.

Figure 4: Example of a workspace slice with reachable poses indicated by dark pixels.

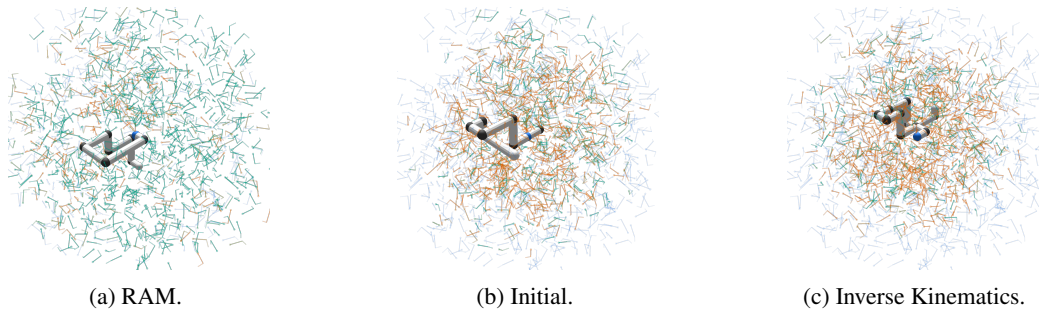


Figure 5: Result of a morphology optimisation compared to the initial morphology. Task poses are displayed in opaque blue, whereas the actually reached poses fade from green (for close, reachable poses) to red for (poses far away or in self-collision).

pare against implicit differentiation directly through a numerical solver for inverse kinematics [51]. Our approach maximised the predicted reachability via Adam [52], while the baseline minimised the mean pose error  $\|\mathbf{P} - f(\mathbf{M}, f^{-1}(\mathbf{M}, \mathbf{P}))\|_{\text{SE}(3)}$  and self-collisions via Limited-memory BFGS [53]. Section L details the loss formulations and reports additional results.

*Gradient-based Morphology Optimisation* We maximised the reachability of random target poses by iteratively modifying link lengths  $\mathbf{a}$  and offsets  $\mathbf{d}$  of an initial morphology, the only continuous Euclidean parameters. At each iteration,  $\mathbf{a}$  and  $\mathbf{d}$  were normalised, squashed to avoid perpetual self-collisions, and renormalised; since squashing only shrinks parameters, the second normalisation cannot require additional squashing. The squashing process was disregarded in the backward pass to avoid non-differentiability. We optimised morphologies over  $10^2$  iterations for  $10^3$  task poses across  $10^2$  seeds. Figure A4 reports the mean pose error and the number of self-collisions, as well as an empirical estimate of the runtime scaling with respect to the number of task poses. Figure 5 shows an optimised morphology.

Both approaches produced substantial improvements over the initial morphology. RAM reduced the mean pose error by about 78%, whereas the baseline achieved a 69% reduction. Both baseline and RAM reduced the proportion of self-collisions from 16% to 6%. The most striking difference was the runtime, where RAM was consistently 1.5 orders of magnitude faster than the baseline.

*Gradient-based Trajectory Optimisation* We also optimised the reachability along a nominal trajectory for a fixed morphology. Since  $\text{SE}(3)$  is not Euclidean, additive gradient updates cannot be trivially applied to poses. Therefore, we optimised an offset vector  $\mathbf{v} \in \mathbb{R}^6$  in tangent space for each waypoint, mapping back to  $\text{SE}(3)$  via the exponential map  $\mathbf{P}_{\text{opt}} = \exp(\mathbf{P}_{\text{nom}}, \mathbf{v})$ . We sampled the nominal trajectory from the geodesic between two random reachable poses and regularised the loss for deviations from the nominal trajectory  $\|\mathbf{P}_{\text{opt}} - \mathbf{P}_{\text{nom}}\|_{\text{SE}(3)}$ . Figure A5 shows the mean pose error, number of self-collisions, and nominal deviation for 10 waypoints over  $10^2$  seeds, as well as an empirical estimate of the runtime scaling with respect to the number of waypoints. Figure A6 shows an optimised trajectory.

Both approaches improved the reachability by deviating from the nominal trajectory. RAM reduced the pose error by 62% and the proportion of self-collisions from 10% to 4%. The baseline deviated three times less than RAM but reduced the pose error by only 51% and the proportion of self-collisions to 3%. For trajectory optimisation, our approach suffered from over-approximation in the training data, leading to overconfident predictions and, as a result, gradients diminishing before arriving at a reachable pose. However, RAM still outperformed the baseline in pose error reduction, while reducing runtime by more than two orders of magnitude.

## 6 Conclusion, Limitations, and Future Work

RAM frames pose reachability as binary occupancy classification, decoupling the existence of an inverse kinematics solution from the harder problem of finding it. RAM generalises across mor-

phologies because the reachable workspace varies more smoothly with kinematic parameters than the inverse kinematics solution set. Three limitations remain: RAM inherits the discretisation error of its training labels, establishing a practical ceiling on representation accuracy; it is restricted to conventional serial manipulators with 5-7 DoF; and the over-approximation in training labels causes gradients to diminish in trajectory optimisation before reaching truly reachable poses. The discretisation ceiling suggests a natural synergy with advances in inverse kinematics solvers, which could provide higher-fidelity labels. Beyond improving label quality, two directions stand out: replacing the sequential encoder with a graph-based alternative to support arbitrary kinematic topologies, and exploiting the differentiable surrogate to jointly optimise morphology and trajectory in a single gradient-based loop, which the sequential nature of current design and planning pipelines precludes.

## Acknowledgments

This work was supported by the Deutsche Forschungsgemeinschaft (German Research Foundation) under grant number AL 1185/31-1, and the DASHH (HELMHOLTZ Graduate School for the Structure of Matter) under grant number HIDSS-0002. The authors gratefully acknowledge the computational and data resources provided by the Leibniz Supercomputing Centre ([www.lrz.de](http://www.lrz.de)). We would also like to thank Olivia Garland for the video voice-over and general advising.

## References

- [1] J. Klzl, S. Ha, and M. Althoff. A Design Co-Pilot for Task-Tailored Manipulators. arXiv:2509.13077, 2025.
- [2] Y. Dai, S. He, X. Nie, X. Rui, S. Li, and S. He. Research on Reconfiguration Strategies for Self-reconfiguring Modular Robots: A Review. *Journal of Intelligent & Robotic Systems*, 110(2), 2024.
- [3] M. Qin, J. Brawer, and B. Scassellati. Robot tool use: A survey. *Frontiers in Robotics and AI*, 9, 2023.
- [4] B. Deroo, B. Pousett, E. Aertbelin, W. Decr, and H. Bruyninckx. The Need for Task-Specific Execution in Robot Manipulation: Skill Design for Energy-Efficient Control. In *IEEE Int. Conf. on Automation Science and Engineering (CASE)*, pages 1–7, 2023.
- [5] S. Schiele, S. Baumgartner, S. Laudahn, and T. C. Lueth. Automated design of task specific additively manufacturable coupled serial chain mechanisms for tracing predefined planar trajectories. In *Proc. of the IEEE/RSJ Int. Conf. on Intelligent Robots and Systems (IROS)*, pages 3047–3052, 2022.
- [6] E. M. Hoffman, D. Costanzi, G. Fadini, N. Miguel, A. D. Prete, and L. Marchionni. Addressing Reachability and Discrete Component Selection in Robotic Manipulator Design Through Kineto-Static Bi-Level Optimization. *IEEE Robotics and Automation Letters*, 10(3):2263–2270, 2025.
- [7] S. Ha, S. Coros, A. Alspach, J. Kim, and K. Yamane. Computational co-optimization of design parameters and motion trajectories for robotic systems. *The International Journal of Robotics Research*, 37(13-14):1521–1536, 2018.
- [8] R. S. Hartenberg and J. Denavit. *Kinematic Synthesis of Linkages*. McGraw-Hill, 1964.
- [9] S. Shirafuji and K. Shimamura. Kinematic Synthesis of a Serial Manipulator Using Gradient-Based Optimization on Lie Groups. *IEEE Robotics and Automation Letters*, 10(3):2550–2557, 2025.
- [10] K. M. Lynch and F. C. Park. *Modern Robotics*. Cambridge University Press, 2017.
- [11] D. L. Pieper. *The Kinematics of Manipulators under Computer Control*. Stanford University, 1969.
- [12] F. Zacharias, C. Borst, and G. Hirzinger. Capturing robot workspace structure: Representing robot capabilities. In *Proc. of the IEEE/RSJ Int. Conf. on Intelligent Robots and Systems (IROS)*, pages 3229–3236, 2007.
- [13] G. Chirikjian and I. Ebert-Uphoff. Numerical convolution on the Euclidean group with applications to workspace generation. *IEEE Transactions on Robotics and Automation*, 14(1): 123–136, 1998.
- [14] N. Vahrenkamp, T. Asfour, G. Metta, G. Sandini, and R. Dillmann. Manipulability analysis. In *Proc. of the IEEE-RAS Int. Conf. on Humanoid Robots (Humanoids)*, pages 568–573, 2012.

- [15] Y. Han, J. Pan, M. Xia, L. Zeng, and Y.-J. Liu. Efficient SE(3) Reachability Map Generation via Interplanar Integration of Intra-planar Convolutions. In *Proc. of the IEEE Int. Conf. on Robotics and Automation (ICRA)*, pages 1854–1860, 2021.
- [16] K. Leibrandt, L. da Cruz, and C. Bergeles. Designing Robots for Reachability and Dexterity: Continuum Surgical Robots as a Pretext Application. *IEEE Transactions on Robotics*, 39(4): 2989–3007, 2023.
- [17] V. Sitzmann, J. N. Martel, A. W. Bergman, D. B. Lindell, and G. Wetzstein. Implicit neural representations with periodic activation functions. In *Proc. of the Int. Conf. on Neural Information Processing Systems (NeurIPS)*, pages 7462–7473, 2020.
- [18] L. Mescheder, M. Oechsle, M. Niemeyer, S. Nowozin, and A. Geiger. Occupancy networks: Learning 3D reconstruction in function space. In *Proc. of the IEEE Conf. on Computer Vision and Pattern Recognition (CVPR)*, pages 4460–4470, 2019.
- [19] O. Limoyo, F. Marić, M. Giamou, P. Alexson, I. Petrović, and J. Kelly. Generative Graphical Inverse Kinematics. *IEEE Transactions on Robotics*, 41:1002–1018, 2025.
- [20] R. Diankov. *Automated Construction of Robotic Manipulation Programs*. PhD thesis, Carnegie Mellon University, 2018.
- [21] D. Ostermeier, J. Külz, and M. Althoff. Automatic Geometric Decomposition for Analytical Inverse Kinematics. *IEEE Robotics and Automation Letters*, 10(10):9964–9971, 2025.
- [22] C. Yasutake, Z. Kingston, and B. Plancher. HJCD-IK: GPU-accelerated inverse kinematics through batched hybrid jacobian coordinate descent. arXiv:2510.07514, 2025.
- [23] P. Beeson and B. Ames. TRAC-IK: An open-source library for improved solving of generic inverse kinematics. In *Proc. of the IEEE-RAS Int. Conf. on Humanoid Robots (Humanoids)*, pages 928–935, 2015.
- [24] B. Sundaralingam, S. K. S. Hari, A. Fishman, C. Garrett, K. Van Wyk, V. Blukis, A. Millane, H. Oleynikova, A. Handa, F. Ramos, N. Ratliff, and D. Fox. CuRobo: Parallelized collision-free robot motion generation. In *Proc. of the IEEE Int. Conf. on Robotics and Automation (ICRA)*, pages 8112–8119, 2023.
- [25] T. von Oehsen, A. Fabisch, S. Kumar, and F. Kirchner. Comparison of Distal Teacher Learning with Numerical and Analytical Methods to Solve Inverse Kinematics for Rigid-Body Mechanisms. arXiv:2003.00225, 2020.
- [26] B. Ames, J. Morgan, and G. Konidaris. IKFlow: Generating diverse inverse kinematics solutions. *IEEE Robotics and Automation Letters*, 7(3):7177–7184, 2022.
- [27] R. Bensadoun, S. Gur, N. Blau, and L. Wolf. Neural inverse kinematic. In *Proc. of the Int. Conf. on Machine Learning (ICML)*, pages 1787–1797, 2022.
- [28] K. Abdel-Malek and J. Yang. Workspace boundaries of serial manipulators using manifold stratification. *The International Journal of Advanced Manufacturing Technology*, 28(11): 1211–1229, 2006.
- [29] R. F. Cavelli, P. D. Cen Cheng, and M. Indri. Modeling the Reachability Space of Robotic Manipulators through Ellipsoid Equations. *Journal of Intelligent & Robotic Systems*, 111(3), 2025.
- [30] J. J. Park, P. Florence, J. Straub, R. Newcombe, and S. Lovegrove. DeepSDF: Learning continuous signed distance functions for shape representation. In *Proc. of the IEEE Conf. on Computer Vision and Pattern Recognition (CVPR)*, pages 165–174, 2019.

- [31] B. Mildenhall, P. P. Srinivasan, M. Tancik, J. T. Barron, R. Ramamoorthi, and R. Ng. NeRF: Representing scenes as neural radiance fields for view synthesis. *arXiv:2003.08934*, 2020.
- [32] M. Z. Irshad, M. Comi, Y.-C. Lin, N. Heppert, A. Valada, R. Ambrus, Z. Kira, and J. Tremblay. Neural Fields in Robotics: A Survey. *arXiv:2410.20220*, 2024.
- [33] Y. Li, Y. Zhang, A. Razmjoo, and S. Calinon. Representing Robot Geometry as Distance Fields: Applications to Whole-body Manipulation. *arXiv:2307.00533*, 2024.
- [34] Y. Li, X. Chi, A. Razmjoo, and S. Calinon. Configuration Space Distance Fields for Manipulation Planning. In *Proc. of Robotics: Science and Systems (RSS)*, volume 20, 2024.
- [35] A. Gienger, C. Stein, A. P. R. Lauer, O. Sawodny, and C. Tarín. Data-Based Reachability Analysis and Optimized Robot Positioning for Co-Design of Construction Processes. In *IEEE/SICE Int. Symp. on System Integration (SII)*, pages 1247–1252, 2024.
- [36] M. Murooka, I. Kumagai, M. Morisawa, and F. Kanehiro. Learning Differentiable Reachability Maps for Optimization-Based Humanoid Motion Generation. In *Proc. of the IEEE-RAS Int. Conf. on Humanoid Robots (Humanoids)*, pages 1–8, 2025.
- [37] S. Kim and J. Perez. Learning Reachable Manifold and Inverse Mapping for a Redundant Robot manipulator. In *Proc. of the IEEE Int. Conf. on Robotics and Automation (ICRA)*, pages 4731–4737, 2021.
- [38] X. Chen, J. Külz, and M. Althoff. Generating robot capability maps with neural fields. In *Proc. of Robotics: Science and Systems (RSS)*, 2024.
- [39] E. S. Conkur and R. Buckingham. Clarifying the definition of redundancy as used in robotics. *Robotica*, 15(5):583–586, 1997.
- [40] J. Craig. *Introduction to Robotics*. Pearson International, 2013.
- [41] R. Reiter. On Closed World Data Bases. In H. Gallaire and J. Minker, editors, *Logic and Data Bases*, pages 55–76. Springer US, 1978.
- [42] N. W. Johnson. *Geometries and Transformations*. Cambridge University Press, 2018.
- [43] Y. Zhou, C. Barnes, J. Lu, J. Yang, and H. Li. On the Continuity of Rotation Representations in Neural Networks. In *Proc. of the IEEE Conf. on Computer Vision and Pattern Recognition (CVPR)*, pages 5738–5746, 2019.
- [44] S. Hochreiter and J. Schmidhuber. Long Short-Term Memory. *Neural Computation*, 9(8):1735–1780, 1997.
- [45] M. Schuck, A. von Rohr, and A. P. Schoellig. Scipy.spatial.transform: Differentiable Framework-Agnostic 3D Transformations in Python. In *Proc. of the Int. Conf. on Neural Information Processing Systems (NeurIPS)*, 2025.
- [46] C. Spearman. The proof and measurement of association between two things. *The American Journal of Psychology*, 15(1):72–101, 1904.
- [47] N. Mantel. The detection of disease clustering and a generalized regression approach. *Cancer research*, 27(2):209–220, 1967.
- [48] K. Simonyan, A. Vedaldi, and A. Zisserman. Deep inside convolutional networks: Visualising image classification models and saliency maps. In *Proc. of the Int. Conf. on Learning Representations (ICLR)*, 2014.
- [49] A. Dosovitskiy and T. Brox. Inverting visual representations with convolutional networks. In *Proc. of the IEEE Conf. on Computer Vision and Pattern Recognition (CVPR)*, pages 4829–4837, 2016.

- [50] A. Mahendran and A. Vedaldi. Understanding deep image representations by inverting them. In *Proc. of the IEEE Conf. on Computer Vision and Pattern Recognition (CVPR)*, pages 5188–5196, 2015.
- [51] J. Rader, T. Lyons, and P. Kidger. Optimistix: Modular optimisation in JAX and Equinox. arXiv:2402.09983, 2024.
- [52] D. P. Kingma and J. Ba. Adam: A method for stochastic optimization. In *Proc. of the Int. Conf. on Learning Representations (ICLR)*, 2015.
- [53] D. C. Liu and J. Nocedal. On the limited memory BFGS method for large scale optimization. *Mathematical Programming*, 45(1):503–528, 1989.
- [54] T. Yoshikawa. Analysis and control of robot manipulators with redundancy. In *Proc. of the Int. Symp. on Robotics Research (ISRR)*, pages 735–747, 1983.
- [55] M. E. Muller. A note on a method for generating points uniformly on n-dimensional spheres. *Communications of the ACM*, 2(4):19–20, 1959.
- [56] K. Shoemake. Uniform random rotations. In *Graphics Gems III*, pages 124–132. Academic Press Professional, Inc., 1992.
- [57] F. C. Park. Distance Metrics on the Rigid-Body Motions with Applications to Mechanism Design. *Journal of Mechanical Design*, 117(1):48–54, 1995.
- [58] M. Žefran, V. Kumar, and C. Croke. Choice of Riemannian Metrics for Rigid Body Kinematics. In *Proc. of the ASME Biennial Mechanisms Conf.*, 1996.
- [59] T. Akiba, S. Sano, T. Yanase, T. Ohta, and M. Koyama. Optuna: A Next-generation Hyperparameter Optimization Framework. In *Proceedings of the 25th ACM (SIGKDD) International Conference on Knowledge Discovery & Data Mining*, pages 2623–2631, 2019.
- [60] R. A. Fisher. Frequency distribution of the values of the correlation coefficient in samples from an indefinitely large population. *Biometrika*, 10(4):507–521, 1915.
- [61] P. Jaccard. étude comparative de la distribution florale dans une portion des Alpes et des Jura. *Bull Soc Vaudoise Sci Nat*, 37:547–579, 1901.
- [62] L. Ruff, R. Vandermeulen, N. Goernitz, L. Deecke, S. A. Siddiqui, A. Binder, E. Müller, and M. Kloft. Deep one-class classification. In *Proc. of the Int. Conf. on Machine Learning (ICML)*, volume 80, pages 4393–4402, 2018.
- [63] M. Tancik, P. P. Srinivasan, B. Mildenhall, S. Fridovich-Keil, N. Raghavan, U. Singhal, R. Ramamoorthi, J. T. Barron, and R. Ng. Fourier features let networks learn high frequency functions in low dimensional domains. In *Proc. of the Int. Conf. on Neural Information Processing Systems (NeurIPS)*, pages 7537–7547, 2020.
- [64] V. Saragadam, D. LeJeune, J. Tan, G. Balakrishnan, A. Veeraraghavan, and R. G. Baraniuk. Wire: Wavelet implicit neural representations. In *Proc. of the IEEE Conf. on Computer Vision and Pattern Recognition (CVPR)*, pages 18507–18516, 2023.
- [65] E. Jang, S. Gu, and B. Poole. Categorical reparameterization with gumbel-softmax. In *Proc. of the Int. Conf. on Learning Representations (ICLR)*, 2017.

## A Scissor Self-collisions

Scissor self-collisions arise when adjacent capsules rotate into an anti-parallel configuration through a shared joint, causing their bodies to overlap. For each joint  $i$ , let  $\mathbf{c}_{\text{pre}}$  and  $\mathbf{c}_{\text{post}}$  denote the direction vectors of the closest non-zero capsule proximal and distal to the joint. Joint  $i$  rotates around the  $z$ -axis of its coordinate frame, defining a rotation plane with unit normal  $\mathbf{n}_i$ . A scissor collision is only possible if both capsules lie in this plane; if either has a component along  $\mathbf{n}_i$ , rotating the joint sweeps it out of the plane and no scissor collision can occur. When both capsules lie in the rotation plane, the collision zone is centred on the anti-parallel configuration of  $\mathbf{c}_{\text{post}}$  relative to  $\mathbf{c}_{\text{pre}}$ . The onset of a collision occurs when the tip of the short capsule  $l_{\min} = \min(\|\mathbf{c}_{\text{pre}}\|, \|\mathbf{c}_{\text{post}}\|)$  is exactly  $2r$  from the axis of the other, as illustrated in Figure A1. If  $l_{\min} < 2r$ , this occurs for all joint angles, a perpetual self-collision, motivating the constraint  $a_{i-1} \in \{0\} \cup [2r, 1]$  and  $d_i \in \{0\} \cup [2r, 1]$ .

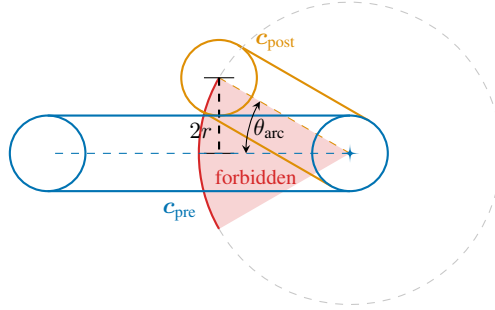


Figure A1: Rotation-plane geometry for joint limit derivation based on scissor-collision-avoidance. The pre-capsule  $\mathbf{c}_{\text{pre}}$  (blue) is fixed; the post-capsule  $\mathbf{c}_{\text{post}}$  (orange) is shown at the boundary of the forbidden arc (red, shaded), where its tip is exactly  $2r$  from the axis of  $\mathbf{c}_{\text{pre}}$ . The forbidden arc spans  $2\theta_{\text{arc}}$  centred on the anti-parallel direction; the joint is restricted to the complementary safe arc of width  $2\pi - 2\theta_{\text{arc}}$ .

## B Details of Morphology Sampling

Since links differ in whether they possess a non-zero length  $a_{i-1}$ , a non-zero offset  $d_i$ , or both, we use four link types  $j \in \{0, 1, 2, 3\}$ : neither, length-only, offset-only, and both. A link with neither offset nor length is essential for constructing co-located joints, such as spherical wrists. Figure 2 displays three link types.

*Link Types* Our hierarchical rejection sampling starts with sampling  $n + 1$  link types  $\mathbf{j}$ , while rejecting consecutive types with neither length nor offset as non-conventional.

*Link Twists* Next, we sample link twists  $\alpha$  ensuring that link types with neither offset nor length obtain a non-zero link twist, and rejecting more than three consecutive parallel or collinear axes as degenerate.

*Link Lengths & Offsets* To preserve distributional uniformity under the constraint  $\sum_i \sqrt{a_i^2 + d_i^2} = 1$ , we sample the link lengths  $\mathbf{a}$  and offsets  $\mathbf{d}$  as

$$\begin{bmatrix} \mathbf{a} \\ \mathbf{d} \end{bmatrix} = \frac{\mathbf{s}}{\|\mathbf{s}\|_1} \begin{bmatrix} \sin \gamma \\ \cos \gamma \end{bmatrix}, \quad \mathbf{s} \stackrel{\text{i.i.d.}}{\sim} \text{Exp}(1), \quad \gamma \stackrel{\text{i.i.d.}}{\sim} \text{Unif}(0, 2\pi), \quad (4)$$

where  $\text{Exp}(1)$  denotes the unit exponential distribution and  $\text{Unif}(0, 2\pi)$  the uniform distribution over  $[0, 2\pi]$ . Link lengths and offsets are rejected if any element is smaller than  $2r$ , as this would lead to perpetual self-collisions between adjacent capsules, as explained in Section A.

*Morphology* Lastly, the complete morphology is rejected if among  $10^3$  randomly sampled joint configurations, see Section C for details, all yield self-collisions or zero Yoshikawa manipulability indices [54] indicating degeneracy. Some examples of resulting morphologies are displayed in Figure 1-I.

## C Sampling of Joint Configurations

We sample all joint configurations except for the end-effector’s  $\theta_{\text{ef}}$ , which is always zero as it is not followed by a subsequent joint, uniformly between joint limits  $\theta_i \sim \text{Unif}[b_l, b_u]$ . Joint limits in this work are not derived from actuator limitations but geometrically to avoid scissor self-collisions as described in Section A, since these are still the most common self-collisions, especially for capsules whose length is roughly  $2r$ . When  $l_{\min} \geq 2r$  the half-arc width of the forbidden zone is  $\theta_{\text{arc}} = \arcsin\left(\frac{2r}{l_{\min}}\right)$  giving a safe range of  $2\pi - 2\theta_{\text{arc}}$  centred on the current safe configuration with offset  $b_u = \phi_0 + \theta_{\text{arc}}$ , where  $\phi_0$  is the angle from  $c_{\text{post}}$  to the anti-parallel direction, so that  $b_l = b_u - (2\pi - 2\theta_{\text{arc}})$ .

## D Uniform Pose Sampling

We sample poses uniformly from  $\mathcal{B}^3(\mathbf{c}, r) \times \text{SO}(3)$ , with centre position  $\mathbf{c}$  and radius  $r$ , by combining a uniformly sampled position  $\mathbf{t} \in \mathcal{B}^3(\mathbf{c}, r)$  and a uniformly sampled orientation  $\mathbf{R} \in \text{SO}(3)$ . The position sampling is [55]

$$\mathbf{t} = \mathbf{c} + \frac{\mathbf{d}}{\|\mathbf{d}\|_2} \cdot r \sqrt[3]{i} \quad i \sim \text{Unif}(0, 1), \quad \mathbf{d} \sim \text{Normal}(\mathbf{0}_3, \mathbf{I}_3) \quad (5)$$

with  $\mathbf{0}_3$  a three dimensional zero vector and  $\mathbf{I}_3$  the  $3 \times 3$  identity matrix. The orientation is then sampled independently as a quaternion [56]

$$\mathbf{q} = \frac{\mathbf{k}}{\|\mathbf{k}\|_2} \quad \mathbf{k} \sim \text{Normal}(\mathbf{0}_4, \mathbf{I}_4) \quad (6)$$

and converted to a rotation matrix [45], yielding the homogeneous transformation matrix

$$\mathbf{P} = \begin{bmatrix} \mathbf{R} & \mathbf{t}^T \\ \mathbf{0} & 1 \end{bmatrix}, \quad (7)$$

which we use as a pose representation throughout the data generation process.

## E Kinematics of Modified Denavit-Hartenberg Parameters

The coordinate transformation of modified Denavit-Hartenberg parameters  $\mathbf{T}_i$  is defined as [40, Eq. 3.6]

$$\mathbf{T}_i = \mathbf{T}(\mathbf{m}_i, \theta_i) = \begin{bmatrix} \cos \theta_i & -\sin \theta_i & 0 & a_{i-1} \\ \sin \theta_i \cos \alpha_{i-1} & \cos \theta_i \cos \alpha_{i-1} & -\sin \alpha_{i-1} & -d_i \sin \alpha_{i-1} \\ \sin \theta_i \sin \alpha_{i-1} & \cos \theta_i \sin \alpha_{i-1} & \cos \alpha_{i-1} & d_i \cos \alpha_{i-1} \\ 0 & 0 & 0 & 1 \end{bmatrix}. \quad (8)$$

The forward kinematics are the cumulative matrix product of coordinate transformations for each link-joint pair and the end effector  $\mathbf{P}_{\text{ef}} = \left(\prod_{i=0}^{n-1} \mathbf{T}_i\right) \mathbf{T}(\mathbf{m}_{\text{ef}}, 0)$ .

## F SE(3) Norm

Due to the nature of floating-point arithmetic, we define a pose as reachable if there exists a joint configuration  $\boldsymbol{\theta} \in \mathcal{T}^n$  such that  $\mathbf{P}_{\text{ef}}$  is within a specified tolerance  $\epsilon$  of the target pose  $\mathbf{P}$

$$\Psi(\mathbf{M}, \mathbf{P}) = \begin{cases} 1 & \text{if } \exists \boldsymbol{\theta} \in \mathcal{T}^n : \|\mathbf{P}_{\text{ef}} - \mathbf{P}\|_{\text{SE}(3)} < \epsilon \\ 0 & \text{else.} \end{cases} \quad (9)$$

Since SE(3) lacks a canonical, bi-invariant metric [57], we weight translational and rotational errors [58, Theorem 4.4]

$$\|\mathbf{P}_1 - \mathbf{P}_2\|_{\text{SE}(3)} = \sqrt{c_1 \|\mathbf{t}_1 - \mathbf{t}_2\|_2^2 + c_2 \|\mathbf{R}_1^T \mathbf{R}_2\|_{\text{SO}(3)}^2} \quad (10)$$

where  $\|\cdot\|_{\text{SO}(3)}$  denotes the geodesic distance. We set  $c_1 = \frac{1}{8}$  and  $c_2 = \frac{1}{2\pi^2}$  to bound both error components to  $\frac{1}{2}$  for translations within the unit ball  $\mathcal{B}^3$ , ensuring both contribute equally to the metric. We set the tolerance to  $\epsilon = 10^{-4}$  to obtain reachability labels.

## G Additional Results for RQ1: Label Fidelity

Table A1 reports the entire binary confusion matrix for the various discretisation granularities. The false positives are decreasing with increasing granularity as expected. However, within the allocated computation time, an increasing number of workspaces are not thoroughly explored, leading to more false negatives.

Table A1: Binary confusion matrix for the tested discretisation granularities.

Cell Distance	DoF	True Positives (%)	False Negatives (%)	False Positives (%)	True Negatives (%)
[0.158, 0.163]	All	$100_{-0}^{+0}$	$0_{-0}^{+0}$	$72_{-5}^{+5}$	$28_{-5}^{+5}$
	7	$100_{-0}^{+0}$	$0_{-0}^{+0}$	$75_{-5}^{+5}$	$25_{-5}^{+5}$
	6	$100_{-0}^{+0}$	$0_{-0}^{+0}$	$76_{-5}^{+5}$	$24_{-5}^{+5}$
	5	$100_{-0}^{+0}$	$0_{-0}^{+0}$	$64_{-6}^{+6}$	$36_{-6}^{+6}$
[0.080, 0.083]	All	$99_{-0}^{+1}$	$1_{-1}^{+0}$	$34_{-5}^{+5}$	$64_{-5}^{+5}$
	7	$98_{-0}^{+1}$	$2_{-1}^{+0}$	$41_{-6}^{+6}$	$59_{-7}^{+6}$
	6	$99_{-0}^{+1}$	$1_{-1}^{+0}$	$33_{-5}^{+4}$	$67_{-4}^{+4}$
	5	$99_{-0}^{+1}$	$1_{-1}^{+0}$	$33_{-5}^{+4}$	$67_{-4}^{+5}$
[0.040, 0.042]	All	$97_{-0}^{+0}$	$3_{-0}^{+0}$	$18_{-3}^{+3}$	$82_{-3}^{+3}$
	7	$96_{-0}^{+0}$	$4_{-0}^{+0}$	$26_{-4}^{+5}$	$74_{-5}^{+4}$
	6	$98_{-0}^{+0}$	$2_{-0}^{+1}$	$13_{-2}^{+2}$	$87_{-2}^{+2}$
	5	$98_{-0}^{+0}$	$2_{-0}^{+0}$	$15_{-3}^{+3}$	$85_{-3}^{+3}$
[0.021, 0.033]	All	$89_{-3}^{+3}$	$11_{-3}^{+3}$	$10_{-2}^{+3}$	$90_{-3}^{+2}$
	7	$82_{-5}^{+6}$	$18_{-6}^{+5}$	$16_{-4}^{+4}$	$84_{-4}^{+3}$
	6	$90_{-3}^{+4}$	$10_{-3}^{+3}$	$6_{-1}^{+2}$	$94_{-2}^{+1}$
	5	$96_{-0}^{+0}$	$4_{-1}^{+0}$	$7_{-2}^{+2}$	$93_{-2}^{+2}$

## H Additional Details of our Reachability Dataset

To generate our dataset at the chosen granularity of [0.040, 0.042], we sampled joint configurations as described in Section C to approximate the workspace according to Section 4.3. On average across batches, 84% of evaluated joint configurations were collision-free, of which 31% filled a previously empty cell, yielding an overall efficiency of 26% for evaluated forward kinematics. This average masks a strong temporal trend: early batches fill new cells at near-unity rate, while later batches increasingly revisit already-covered cells as the workspace saturates, motivating the frontier-guided sampling strategies discussed in Section M. We empirically determined the number of samples per morphology to  $10^6$ , the threshold at which RAM, trained on a single morphology, successfully generalised to unseen poses of that same morphology. The number of morphologies in the training set was increased as much as possible within our computational budget.

The resulting large-scale reachability dataset contains samples for  $3 \cdot 10^4$  morphologies, split equally into  $10^4$  morphologies of five, six, and seven DoF. Using the sampling from Section 4.1, about 38% of morphologies possess analytically solvable inverse kinematics. The vast majority of these have five DoF, as virtually all possess analytically solvable kinematics given our morphological constraints. To balance the reachability classes for these manipulators with five DoF, we sample 25% of their poses from the configuration space as  $f(\mathbf{M}, \boldsymbol{\theta})$  with  $\boldsymbol{\theta}$  according to Section C. The entire dataset consists of 29% reachable poses. The dataset is 202GB and took 360 GPU hours to generate on an Nvidia H100.

To obtain boundary poses, we sample  $10^2$  pairs of reachable poses  $P_r$  and unreachable poses  $P_u$  from the dataset. We sample the geodesic between the poses with  $10^2$  samples each, using the tangent vector  $\mathbf{g} = \log(P_r, P_u)$  and the exponential map to compute the  $i$ -th sample as

$$P_i = \exp\left(P_r, \frac{i}{100} \cdot \mathbf{g}\right) \quad (11)$$

resulting in  $10^4$  boundary samples per split ( $10^2$  pairs  $\times$   $10^2$  geodesic samples).

## I Workspace Slices

We create the visualisation in Figure 4 by fixing the orientation and one positional variable while varying the remaining two in a grid. To obtain slices that intersect the workspace, we start from a morphology  $M$  and compute its estimated workspace centre  $\mathbf{t}_0$  and radius  $r_{\text{mov}} = 1 - \|\mathbf{t}_0\|_2 - \|\mathbf{t}_{\text{eff}}\|_2$ . We take the central position as the slice centre. The displayed orientation is chosen from the pose with the median Euclidean distance from the centre position. The displayed plane is the rotation plane of the first joint, which we determine by computing the transformation matrix  $\mathbf{T}_0(\mathbf{m}_0, \mathbf{0}) = \begin{bmatrix} \mathbf{R}_0 & \mathbf{t}_0^T \\ \mathbf{0} & 1 \end{bmatrix}$  and extracting the third column of its rotation matrix  $(R_0)_{:,3}$ . We sample each remaining positional variable with  $10^3$  uniformly spaced values for a total of  $10^6$  samples.

## J Hyperparameters

Table A2 displays the hyperparameters of our classifier and the training routine, which were the result of a hyperparameter sweep [59] on a fraction of the training set.

Table A2: Hyperparameters of the classifier and the training.

Parameter	Value
LSTM latent embedding size	128
LSTM # layers	1
MLP hidden layer size	1792
MLP # layers	8
Epochs	1
Batch size	1000
Optimiser	Adam [52]
Learning rate	$3 \cdot 10^{-4}$
$\beta$	(0.9, 0.999)

## K Additional Details for RQ2: Accuracy of RAM

Table A3 reports the full binary confusion matrices for the validation set and the various isolated DoF, where we evaluated GGIK only on the validation set due to the slow inference. Moreover, Figure A2 visualises the out-of-distribution capabilities of RAM by showing the  $F_1$ -Scores on random and boundary datasets split by DoF.

Table A3: Comparison of RAM and GGIK. We denote the binary confusion matrix with True Positives (TP), False Negatives (FN), False Positives (FP), and True Negatives (TN).

Classifier	DoF	Random (%)				Boundary (%)			
		TP	FN	FP	TN	TP	FN	FP	TN
RAM	{5, 6, 7}	94 <sup>+1</sup> <sub>-1</sub>	6 <sup>+1</sup> <sub>-1</sub>	25 <sup>+2</sup> <sub>-2</sub>	75 <sup>+2</sup> <sub>-2</sub>	98 <sup>+3</sup> <sub>-2</sub>	2 <sup>+2</sup> <sub>-3</sub>	57 <sup>+8</sup> <sub>-8</sub>	43 <sup>+8</sup> <sub>-8</sub>
	1	2 <sup>+2</sup> <sub>-2</sub>	98 <sup>+2</sup> <sub>-2</sub>	0 <sup>+0</sup> <sub>-0</sub>	100 <sup>+0</sup> <sub>-0</sub>	6 <sup>+5</sup> <sub>-5</sub>	94 <sup>+5</sup> <sub>-5</sub>	1 <sup>+1</sup> <sub>-1</sub>	99 <sup>+1</sup> <sub>-1</sub>
	2	28 <sup>+7</sup> <sub>-7</sub>	72 <sup>+7</sup> <sub>-7</sub>	4 <sup>+2</sup> <sub>-2</sub>	96 <sup>+2</sup> <sub>-2</sub>	24 <sup>+10</sup> <sub>-10</sub>	76 <sup>+10</sup> <sub>-10</sub>	4 <sup>+2</sup> <sub>-3</sub>	96 <sup>+3</sup> <sub>-2</sub>
	3	63 <sup>+7</sup> <sub>-8</sub>	37 <sup>+8</sup> <sub>-7</sub>	5 <sup>+2</sup> <sub>-2</sub>	95 <sup>+2</sup> <sub>-2</sub>	66 <sup>+9</sup> <sub>-10</sub>	34 <sup>+10</sup> <sub>-9</sub>	13 <sup>+4</sup> <sub>-4</sub>	87 <sup>+4</sup> <sub>-4</sub>
	4	87 <sup>+4</sup> <sub>-4</sub>	13 <sup>+4</sup> <sub>-4</sub>	8 <sup>+1</sup> <sub>-2</sub>	92 <sup>+2</sup> <sub>-1</sub>	95 <sup>+8</sup> <sub>-5</sub>	5 <sup>+5</sup> <sub>-8</sub>	32 <sup>+8</sup> <sub>-8</sub>	68 <sup>+8</sup> <sub>-8</sub>
	5	91 <sup>+3</sup> <sub>-2</sub>	9 <sup>+2</sup> <sub>-3</sub>	18 <sup>+2</sup> <sub>-2</sub>	82 <sup>+2</sup> <sub>-2</sub>	96 <sup>+8</sup> <sub>-4</sub>	4 <sup>+4</sup> <sub>-8</sub>	59 <sup>+14</sup> <sub>-15</sub>	41 <sup>+15</sup> <sub>-14</sub>
	6	96 <sup>+1</sup> <sub>-1</sub>	4 <sup>+1</sup> <sub>-1</sub>	30 <sup>+3</sup> <sub>-3</sub>	70 <sup>+3</sup> <sub>-3</sub>	99 <sup>+1</sup> <sub>-1</sub>	1 <sup>+1</sup> <sub>-1</sub>	78 <sup>+10</sup> <sub>-9</sub>	22 <sup>+9</sup> <sub>-10</sub>
	7	95 <sup>+1</sup> <sub>-1</sub>	5 <sup>+1</sup> <sub>-1</sub>	27 <sup>+3</sup> <sub>-3</sub>	73 <sup>+3</sup> <sub>-3</sub>	99 <sup>+1</sup> <sub>-1</sub>	1 <sup>+1</sup> <sub>-1</sub>	28 <sup>+11</sup> <sub>-13</sub>	72 <sup>+13</sup> <sub>-11</sub>
	8	91 <sup>+2</sup> <sub>-1</sub>	9 <sup>+1</sup> <sub>-2</sub>	32 <sup>+3</sup> <sub>-3</sub>	68 <sup>+3</sup> <sub>-3</sub>	94 <sup>+4</sup> <sub>-3</sub>	6 <sup>+3</sup> <sub>-4</sub>	56 <sup>+8</sup> <sub>-8</sub>	44 <sup>+8</sup> <sub>-8</sub>
	9	80 <sup>+2</sup> <sub>-2</sub>	20 <sup>+2</sup> <sub>-2</sub>	25 <sup>+2</sup> <sub>-2</sub>	75 <sup>+2</sup> <sub>-2</sub>	87 <sup>+4</sup> <sub>-4</sub>	13 <sup>+4</sup> <sub>-4</sub>	52 <sup>+8</sup> <sub>-8</sub>	48 <sup>+8</sup> <sub>-8</sub>
GGIK	{5, 6, 7}	90 <sup>+1</sup> <sub>-1</sub>	10 <sup>+1</sup> <sub>-1</sub>	62 <sup>+2</sup> <sub>-2</sub>	38 <sup>+2</sup> <sub>-2</sub>	94 <sup>+4</sup> <sub>-3</sub>	6 <sup>+3</sup> <sub>-4</sub>	78 <sup>+5</sup> <sub>-5</sub>	22 <sup>+5</sup> <sub>-5</sub>
	7	88 <sup>+3</sup> <sub>-2</sub>	12 <sup>+2</sup> <sub>-3</sub>	60 <sup>+3</sup> <sub>-3</sub>	40 <sup>+3</sup> <sub>-3</sub>	92 <sup>+4</sup> <sub>-3</sub>	8 <sup>+3</sup> <sub>-4</sub>	73 <sup>+11</sup> <sub>-9</sub>	27 <sup>+9</sup> <sub>-11</sub>
	6	90 <sup>+2</sup> <sub>-2</sub>	10 <sup>+2</sup> <sub>-2</sub>	65 <sup>+3</sup> <sub>-3</sub>	35 <sup>+3</sup> <sub>-3</sub>	95 <sup>+5</sup> <sub>-4</sub>	5 <sup>+4</sup> <sub>-5</sub>	84 <sup>+7</sup> <sub>-7</sub>	16 <sup>+7</sup> <sub>-7</sub>
	5	92 <sup>+2</sup> <sub>-2</sub>	8 <sup>+2</sup> <sub>-2</sub>	60 <sup>+4</sup> <sub>-4</sub>	40 <sup>+4</sup> <sub>-4</sub>	96 <sup>+8</sup> <sub>-4</sub>	4 <sup>+4</sup> <sub>-8</sub>	73 <sup>+11</sup> <sub>-10</sub>	27 <sup>+10</sup> <sub>-11</sub>

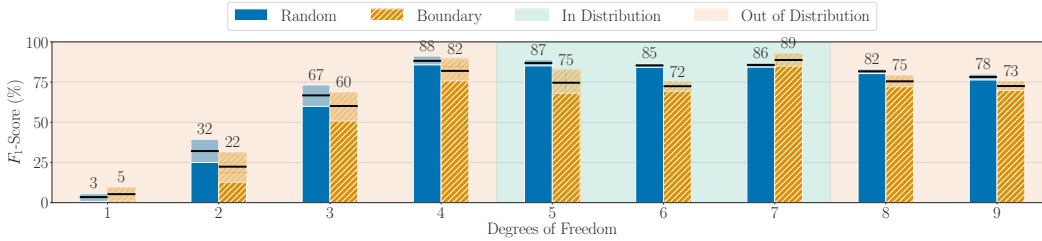


Figure A2:  $F_1$ -score of RAM for random and boundary poses depending on the degrees of freedom in- and out of distribution.

To explore correlations between the latent space and individual morphological attributes, we sampled  $3 \cdot 10^3$  morphologies ( $10^3$  each of five, six, and seven DoF), extracted their LSTM latent vectors, and applied standardised PCA. For each attribute, we computed the Spearman correlation coefficient [46] and the corresponding  $p$ -value for each principal component, retaining the component with the maximum absolute correlation. Confidence intervals were obtained via the Fisher- $z$  transform [60]. To investigate pairwise structural similarities, we sampled  $3 \cdot 10^2$  morphologies ( $10^2$  each of five, six, and seven DoF) and computed pairwise  $300 \times 300$  matrices: cosine similarity and Euclidean distance of latent embeddings; Euclidean distance of the flattened, column-standardised modified Denavit-Hartenberg parameter for input similarity; and a Monte Carlo estimate of the Jaccard index [61] for workspace similarity, where both morphologies evaluate reachability via inverse kinematics for all  $2 \cdot 10^3$  poses, comprising  $10^3$  plausible poses sampled according to Section 4.2 from each morphology. Mantel tests [47] were applied to the upper triangular entries of each matrix pair, with  $p$ -values from row/column permutations and 95% confidence intervals via bootstrapping. Table A4 lists all correlation coefficients, confidence intervals, and  $p$ -values; Figure A3 displays scatter plots of selected attributes against their most correlated principal component, and pairwise latent similarities against input and workspace similarities.

Table A4: Spearman correlation coefficients (SCC) between morphological attributes and the most correlated principal component of the latent space, and Mantel test correlations between pairwise similarity matrices.

<b>Attribute</b>	<b>SCC (%)</b>	<b>p-value</b>
DoF $n$	$86_{-1}^{+1}$	<0.001
Moveable Length $r_{\text{mov}}$	$24_{-3}^{+4}$	<0.001
Base Twist $\alpha_0$	$17_{-4}^{+4}$	<0.001
Base Length $a_0$	$56_{-2}^{+3}$	<0.001
Base Offset $d_0$	$23_{-4}^{+3}$	<0.001
First Twist $\alpha_1$	$10_{-3}^{+4}$	<0.001
First Length $a_1$	$30_{-3}^{+4}$	<0.001
First Offset $d_1$	$11_{-3}^{+4}$	<0.001
EEF Twist $\alpha_n$	$39_{-3}^{+3}$	<0.001
EEF Length $a_n$	$37_{-3}^{+3}$	<0.001
EEF Offset $d_n$	$44_{-3}^{+3}$	<0.001
Reachability $\frac{\sum_i^{1000} l_i}{1000}$	$55_{-3}^{+2}$	<0.001
Centre X $(\mathbf{t}_0)_x$	$56_{-2}^{+3}$	<0.001
Centre Y $(\mathbf{t}_0)_y$	$33_{-3}^{+3}$	<0.001
Centre Z $(\mathbf{t}_0)_z$	$29_{-4}^{+3}$	<0.001
Centre Magnitude $\ \mathbf{t}_0\ _2$	$45_{-3}^{+3}$	<0.001
Min. Link Length $\min_i \sqrt{a_i^2 + d_i^2}$	$19_{-3}^{+4}$	<0.001
Max. Link Length $\max_i \sqrt{a_i^2 + d_i^2}$	$48_{-3}^{+2}$	<0.001
Std. Link Length $\sigma\left(\sqrt{a_i^2 + d_i^2}\right)$	$58_{-2}^{+2}$	<0.001
Fraction Type 0 $\frac{\sum_i \mathbb{1}(j_i=0)}{n}$	$21_{-4}^{+3}$	<0.001
Fraction Type 1 $\frac{\sum_i \mathbb{1}(j_i=1)}{n}$	$30_{-3}^{+4}$	<0.001
Fraction Type 2 $\frac{\sum_i \mathbb{1}(j_i=2)}{n}$	$28_{-3}^{+3}$	<0.001
Fraction Type 3 $\frac{\sum_i \mathbb{1}(j_i=3)}{n}$	$30_{-4}^{+3}$	<0.001
Max. Pos. Type 3 $\max_i \mathbb{1}(j_i = 3)$	$19_{-3}^{+3}$	<0.001
<i>Mantel test</i>		
$d_{\text{MDH}}$ vs. $d_{\text{latent}}$	$34_{-9}^{+10}$	<0.001
$s_{\text{workspace}}$ vs. $s_{\text{latent}}$	$28_{-8}^{+11}$	<0.001

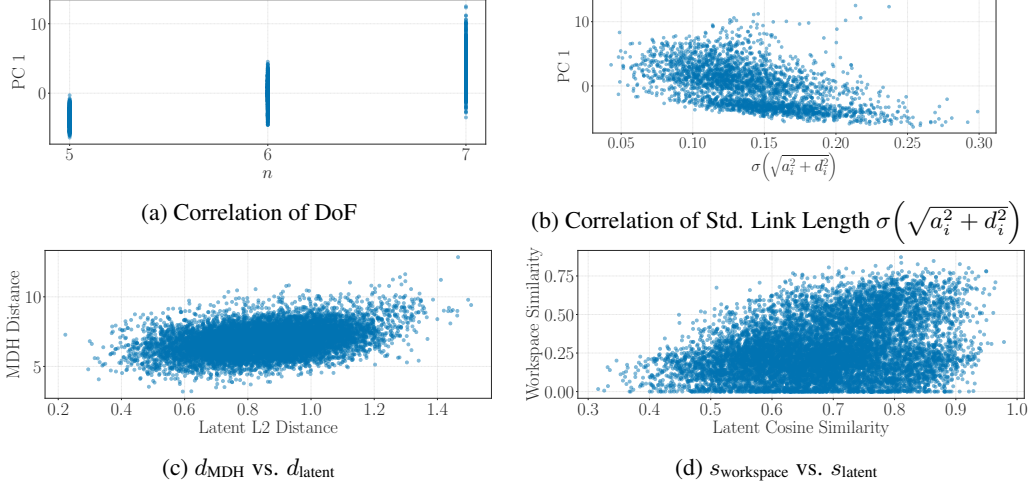


Figure A3: Scatter plots of selected attributes against their most correlated principal component (a,b), and pairwise latent similarities against input and workspace similarities (d,c).

## L Additional Details for RQ3: Practical Utility

*Morphology optimisation.* We optimised the morphology  $M$  with six DoF by maximising predicted reachability over a set of  $N$  random target poses  $\{\mathbf{p}_0, \dots, \mathbf{p}_N\}$ :

$$\max_M \frac{1}{N} \sum_i \text{RAM}(M, \mathbf{p}_i). \quad (12)$$

The baseline minimises a pose-error and self-collision loss via the implicit function theorem applied to a numerical inverse kinematics solver:

$$\min_M \frac{1}{N} \sum_i \max\left(0, \|\mathbf{P}_i - f(M, f^{-1}(M, \mathbf{P}_i))\|_{\text{SE}(3)} - \epsilon\right) + \lambda c(M, f^{-1}(M, \mathbf{P}_i)), \quad (13)$$

where  $\epsilon = 10^{-4}$  is the SE(3) tolerance from Section F, and  $\lambda = 10^4$  is a fixed penalty weight chosen to dominate the pose-error term whenever a self-collision occurs. Figure A4 shows the results over all iterations and the runtime scaling.

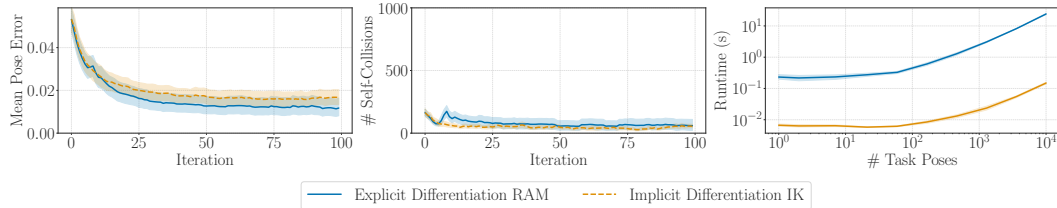


Figure A4: Comparison of morphology-optimisation approaches with regards to quality and runtime.

*Trajectory optimisation.* The trajectory optimisation objective minimises the same RAM loss over the tangent vectors  $\mathbf{V}$  rather than the morphology  $M$ , which are fixed at an initial six DoF morphology:

$$\max_{\mathbf{V}} \frac{1}{N} \sum_i \text{RAM}(M, \mathbf{p}_i), \quad (14)$$

where  $\mathbf{P}_i = \exp(\mathbf{P}_{\text{nom},i}, \mathbf{v}_i)$ ,  $\mathbf{p}_i$  is the vectorised representation of  $\mathbf{P}_i$ ,  $\mathbf{V}$  collects the tangent vectors  $\{\mathbf{v}_i\}$  into a matrix, and  $\mathbf{P}_{\text{nom},i}$  is the  $i$ -th waypoint on the nominal trajectory. The baseline minimises

the same loss as in design optimisation over  $V$  instead:

$$\min_V \frac{1}{N} \sum_i \max(0, \|P_i - f(M, f^{-1}(M, P_i))\|_{SE(3)} - \epsilon) + \lambda c(M, f^{-1}(M, P_i)). \quad (15)$$

Figure A5 shows the results over all iterations and the runtime scaling. Figure A6 shows an example of a nominal trajectory optimised with both methods.

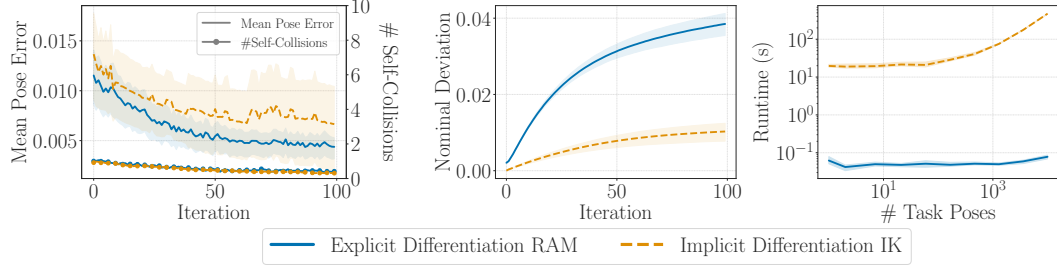


Figure A5: Comparison of trajectory-optimisation approaches with regards to quality and runtime.

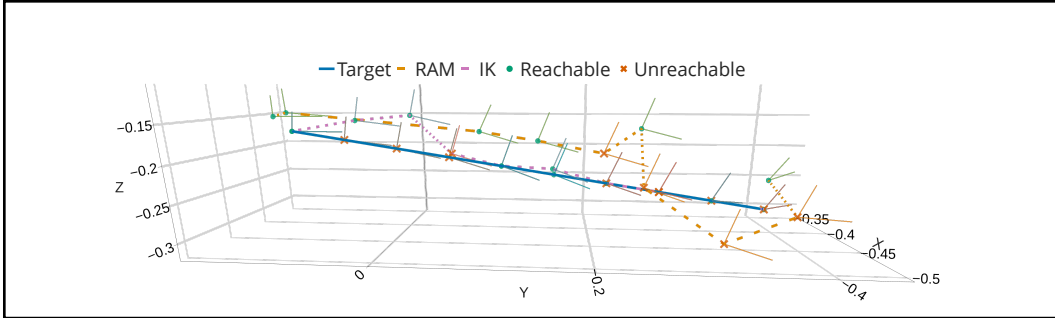


Figure A6: Trajectory optimisation via RAM and inverse kinematics (IK).

## M Negative Results

*Deep one-class classification.* Since reachable poses are substantially cheaper to generate than unreachable poses, we experimented with training solely from reachable samples via deep one-class classification [62], which fits a hypersphere to the data and minimises its volume. The method failed to learn a useful classifier, likely because unreachable poses constitute the majority class and the decision boundary could not be inferred from positive samples alone.

*Fourier feature embeddings.* To improve the representation of high-frequency workspace boundaries, we applied Fourier feature embeddings to the pose input [63]. This did not improve accuracy or convergence, suggesting the MLP has sufficient capacity to represent the relevant frequencies at the resolutions we consider.

*Neural representation architectures.* We evaluated several established implicit neural representation architectures as alternatives to our MLP decoder, including the CNN-based decoder of Occupancy Networks [18], SIREN [17], and WIRE [64]. The ONet decoder is motivated by the Euclidean structure of  $\mathbb{R}^3$ , which is mismatched to our  $SE(3)$  input space. SIREN and WIRE use periodic and Gabor wavelet activations, respectively, to capture high-frequency signals, but offered no benefit over ReLU activations at the resolutions we consider, consistent with our finding that Fourier feature embeddings also did not help. All alternatives performed worse or trained more slowly than the plain MLP decoder we ultimately adopted.

*Frontier-guided configuration sampling.* Rather than sampling joint configurations uniformly to approximate the workspace for Section 4.3, we explored strategies that preferentially generate configurations likely to reach uncovered cells, including Sobol sequences and perturbations of configurations that had previously expanded the covered frontier. All such strategies are more expensive

per sample than uniform sampling and require tuning a perturbation scale that is difficult to set due to the highly non-linear mapping from joint space to  $SE(3)$ . None accelerated workspace approximation over tuned uniform sampling.

*Joint design of discrete and continuous morphology parameters.* For design optimisation, we explored jointly optimising the discrete link twists  $\alpha$  alongside the continuous link lengths using the Gumbel-softmax trick [65] to obtain approximate gradients through the discrete choices. This did not converge, likely because the model does not generalise to twist values outside the training distribution, making early gradients of  $\alpha$  uninformative.